Structural Durability & Health Monitoring

Tech Science Press

Doi:10.32604/sdhm.2026.075676

ARTICLE

Analysis on Impact Resistance of Smart CFRP Laminates with Embedded/Surface-Bonded FBG Sensors

You-Yong Tang[1], Yong-Hao Liu[2], Dong-Yang Wei[1], Xiao-Wei Feng[2], Jose Campos e Matos[3], David Hui[4] and Hua-Ping Wang[1,*]

[1]School of Civil Engineering and Mechanics, Lanzhou University, Lanzhou, China
[2]Gansu Provincial Transportation Research Institute Group Co., Ltd., Lanzhou, China
[3]Department of Civil Engineering, University of Minho, ISISE, Guimarães, Portugal
[4]Department of Mechanical Engineering, The University of New Orleans, New Orleans, LA, USA

*Corresponding Author: Hua-Ping Wang. Email: wanghuaping1128@sina.cn or hpwang@lzu.edu.cn

Received: 06 November 2025; Accepted: 30 December 2025; Published: 18 May 2026

ABSTRACT: Carbon fiber reinforced polymer (CFRP) laminates are widely used in aerospace, new energy, and transportation engineering due to their high specific strength and stiffness. However, interlaminar delamination damage can lead to sudden structural failure, and the occurrence and prediction of such hidden defects are difficult to identify and evaluate using conventional inspection methods. To address this, smart CFRP laminates integrated with fiber Bragg grating (FBG) sensors offer a new approach for real-time structural health monitoring (SHM). Nevertheless, the influence mechanisms of the two integration methods—embedded and surface-bonded FBG sensors—on the static strength and impact resistance of the structure remain unclear. To fill this gap, this paper systematically investigates the mechanical behavior under static and dynamic loads and the optimization strategies for impact resistance of smart CFRP laminates with embedded/surface-bonded FBG sensors through a combination of experimental and simulation methods. Orthogonally laid-up CFRP laminates were designed and fabricated, integrated with FBG sensor arrays to form a primary self-sensing system. The strain characteristics of the CFRP laminate structures with different FBG integration methods were quantitatively analyzed through static loading and low-velocity impact tests. Furthermore, a multi-scale finite element model was established based on LS-DYNA to validate the experimental trends and reveal the underlying mechanisms. The research results indicate that the strain amplitude decays inversely with the distance from the sensor to the loading point, the strain response exhibits typical "four-stage characteristics," the peak strain is positively correlated with the impact energy, and it decays exponentially with sensor distance. The finite element simulations show high consistency with the experimental strain trends, verifying the reliability of the established multi-scale model. Within the linear-elastic, non-damaging regime considered in this study, the finite element simulations indicate that embedded optical fibers slightly redistribute the local stress field but have only a limited influence on the global impact response of the CFRP laminate. These findings provide scientific instruction for the development of smart CFRP structures and the configuration of FBG-based SHM system.

KEYWORDS: Smart CFRP laminate; FBG sensor; SHM; impact resistance; damage mechanism

1 Introduction

Carbon fiber reinforced polymer (CFRP) composites are widely used in aerospace, new energy, and transportation engineering structures due to their high specific strength and stiffness [1–3]. However, the inherent characteristics of CFRP laminates, such as interlaminar degradation and delamination, pose

significant challenges to structural operational safety [4,5]. Such concealed micro-damage is often difficult to detect by visual inspection and may lead to sudden structural failure under service loads. Traditional non-destructive testing methods [6–9] lack real-time capability. In contrast, integrating smart CFRP structures by embedding or surface-bonding optical fiber sensing elements enables real-time, continuous, and long-term stable monitoring of the internal mechanical performance of CFRP structures [10–13], without affecting structural performance. Optical fiber sensors offer advantages such as small size, light weight, immunity to electromagnetic interference, absolute measurement, fire and explosion resistance, corrosion resistance, and ease of forming multiplexed sensor networks. They can be embedded within composite materials to form smart composite structures, sensing structural strain and the spatiotemporal evolution of micro-damage, thus holding significant potential for health monitoring of composite structures [14–18].

Scholars domestically and internationally have conducted research on monitoring and identifying the service or damage status of CFRP laminate structures using surface-bonded or embedded fiber Bragg grating (FBG) sensors [19]. Yashiro et al. used embedded FBG sensing technology to predict various damage states in composite laminates [20]. Liu and Liang quantified the interfacial shear strength of embedded optical fibers in CFRP by using single-fiber pull-out tests, and discussed how interfacial debonding can influence the mechanical performance of smart composite laminates [21]. Under dynamic loads, signals from embedded and surface-bonded FBG arrays can corroborate each other in amplitude, enabling stable acquisition of dynamic responses and achieving high-accuracy damage identification. Lu et al. used FBG sensors to study damage identification methods for CFRP structures, achieving an accuracy rate of over 90%, providing a reliable method for damage assessment of CFRP composite structures [22]. Geng et al. experimentally investigated the sensing characteristics by embedding FBG sensors into CFRP laminates, showing that embedded FBGs can sensitively and stably monitor temperature and strain changes during experiments, with good consistency compared to surface-bonded FBG sensors [23]. Integrating FBGs with prepreg during the manufacturing stage not only allowed online monitoring of resin curing and modulus evolution but also significantly improved survival rate of sensors through reasonable lead-out and packaging, laying a process foundation for impact sensitivity and long-term stability during service [24]. Rocha et al. explored the optimal sensor layout of FBG sensors embedded in CFRP laminates for impact damage identification [25]. In summary, the packaging and installation methods of FBG sensors significantly influence the measurement of strain and temperature in CFRP structures. Test requirements must be fully considered when designing the configuration and installation mode of FBG sensors to ensure test effectiveness, reliability, and long-term stability [26–28].

Some scholars have also used finite element methods such as ABAQUS and ANSYS/LS-DYNA to simulate the response and damage modes of CFRP plates under low-velocity and high-velocity impact, providing scientific reference for closed-loop "experiment-simulation-monitoring mechanism" research. Giannaros et al. used LS-DYNA to study the hypervelocity impact response of CFRP composites, extending the established numerical analysis method to hypervelocity impact problems of CFRP composites and investigating material ballistic limit characteristics and impact crater morphology [29]. Liu et al. used LS-DYNA to study the dynamic response and resistance mechanism of reinforced concrete columns strengthened with CFRP composites under lateral impact loading [30]. Heimbs et al. used LS-DYNA to simulate the effect of compressive preload on the low-velocity impact behavior of three different CFRP composites [31]. Dhaliwal and Newaz. used a combination of experiment and LS-DYNA to study the progressive damage failure modes of Hybrid Composite laminates formed by aluminum and CFRP composites under bending loads [32]. Khan and Sharma developed a progressive damage model with interface delamination for cross-ply laminates subjected to low-velocity impact, highlighting the importance of accurately capturing damage initiation and growth in impact simulations [33]. In summary, based on finite element simulation analysis, combined

with experimental testing, the mechanical properties and failure characteristics of CFRP structures can be effectively and accurately explored. Therefore, it is feasible to further combine structural health monitoring methods to explore the load-bearing performance and damage evolution mechanisms of CFRP structures during service.

The method of embedding FBG sensing elements may affect the local stiffness and interfacial shear stress transfer path of CFRP plates, induce micro-defects, and cause systematic bias in wave velocity, dispersion, and energy attenuation. Using surface-bonded FBG sensing elements does not affect the CFRP plate structure, but its test sensitivity and long-term stability are influenced by the environment and load history. Currently, there is limited research on the long-term effects of embedded FBG sensors on the structural characteristics of CFRP laminates, and a corresponding analysis of the effectiveness of structural health monitoring (SHM) systems is lacking. Therefore, it is necessary to conduct parallel quantitative comparative studies from three dimensions: "impact on the structure itself—sensing reliability—energy assessment accuracy."

Given the foregoing analysis, this study analyzes and compares the structural performance of CFRP plates with surface-bonded and embedded FBG sensing elements under static and dynamic impact loads through experiments and numerical simulation. It evaluates the impact of these two smart CFRP laminates integration methods on structural response and the ability of FBG sensors to monitor the strain or damage of the CFRP laminates. The main contributions of this study are:

(1) Established a comparative framework for evaluating the effects of surface-bonded and embedded FBG integration methods on assessing mechanical performance of CFRP laminates and effectiveness of the configured SHM system.
(2) Proposed a static-impact collaborative testing method, revealing the regularity and applicability of FBG responses.
(3) Constructed and validated a high-fidelity LS-DYNA multi-scale finite element model, providing a quantifiable basis for selecting appropriate FBG integration schemes for different engineering requirements.

The main structure of the paper contains five sections. Section 1 declares the current progress on the smart CFRP laminates assembled with optical fiber sensing elements. Section 2 describes the FBG sensing principle, specimen preparation, sensor layout, calibration and measurement procedures. Section 3 presents the experimental system and data processing workflow, as well as the static loading and low-velocity impact tests. Section 4 develops and validates the numerical model, compares simulations with experiments, and quantifies the effects of embedded and surface-bonded configurations on structural response and energy assessment. Section 5 summarizes the main conclusions and discusses engineering implications.

2 Smart CFRP Laminates Assembled with FBG Sensing Elements

This section summarizes the key technologies and design considerations for developing smart CFRP laminates fused with FBG sensing techniques. It firstly outlines the operation principles of FBG sensors, and then discusses approaches for integrating FBGs into CFRP laminates, the associated challenges, and practical design guidelines.

2.1 Working Principles of FBG Sensing Element

Optical fibers used for sensing consist of a core, cladding, and protective coating (Fig. 1), which deform together under external loading. In practice, interfacial debonding or slippage among the core, cladding, and coating is undesirable because it degrades strain transfer and can trigger local stress concentrations

and premature failure. The core and cladding are silica and form the effective sensing element. The protective coating is an organic polymer; it may absorb a small fraction of strain and thus introduce a minor measurement bias during testing. However, because the coating thickness is only 62.5 μm relative to engineering length scales, its influence on the measured strain is commonly neglected. Accordingly, the fiber is modeled as a single layer with an effective radius of 125 μm [34].

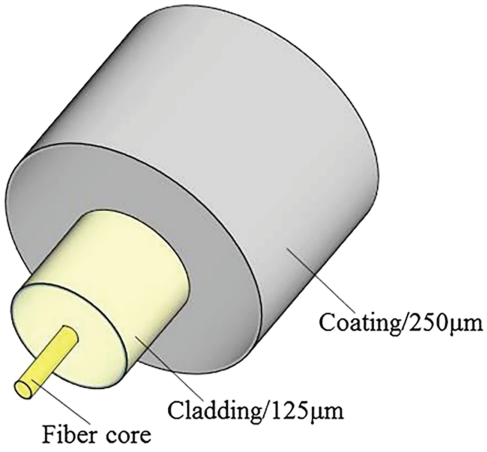

Figure 1: Structure of bare optical fiber sensing element

Under a constant temperature (T), applying a finite strain to the FBG alters the grating pitch in the grating region and/or the effective refractive index (n_{eff}). This leads to a shift of the Bragg wavelength ($\Delta\lambda_B$), which is readily measurable. From the magnitude of this shift, the applied strain can be directly estimated, and its tensile or compressive nature can be identified. Considering the applied uniaxial strain (ε) and the change in operating temperature (ΔT), $\Delta\lambda_B$ can be estimated as:

$$\Delta\lambda_B = 2\left[\Lambda\frac{\partial n_{eff}}{\partial L} + n_{eff}\frac{\partial\Lambda}{\partial L}\right]\Delta L + 2\left[\Lambda\frac{\partial n_{eff}}{\partial T} + n_{eff}\frac{\partial\Lambda}{\partial T}\right]\Delta L \tag{1}$$

Assuming $\Delta T = 0$, the linear-elastic regime of Eq. (1) is:

$$\Delta\lambda_B = \lambda_B\left(1-\rho_e\right)\varepsilon \tag{2}$$

where ρ_e is the effective elasto-optic constant, which can be expressed as:

$$\rho_e = \frac{n_{eff}^2}{2}\left(\rho_{12} - \sigma\left(\rho_{11}+\rho_{12}\right)\right) \tag{3}$$

where ρ_{11} and ρ_{12} are coefficients of the elasto-optic tensor, and σ is the Poisson's ratio. For a typical SMF made of SiO_2, the values are $\rho_{12} = 0.252$, $\rho_{11} = 0.113$, and $n_{eff} = 1.482$, respectively. Both $\Delta\lambda_B$ and the grating-plane period vary with temperature, which in turn alters λ_B. The wavelength shift with respect to temperature ΔT can be expressed as [35]:

$$\Delta\lambda_B = \lambda_B\left(\beta_T + \zeta\right)\Delta T \tag{4}$$

where $\beta_T \simeq 0.55\times10^{-6}$ is the thermal expansion coefficient, and $\zeta = 8.6\times10^{-6}$ is the thermo-optic coefficient. Accordingly, the thermal sensitivity of λ_B is approximately 13.7 pm/°C. Finally, the sensitivity of the

FBG sensor induced by strain and temperature variation can be expressed as [36]:

$$\frac{\Delta\lambda_B}{\lambda_B} = (1-\rho_e)\,\varepsilon + (\beta_T + \zeta)\,\Delta T \tag{5}$$

From Eq. (5), it can be seen that $\Delta\lambda_B$, ε, and ΔT are interrelated. Therefore, thermal compensation is required for measuring the strain of the monitored structure. If the temperature variation is neglected, which means that the second term of Eq. (5) is zero, the FBG wavelength shift is linearly proportional to the structural strain. Based on calibration experiments, the approximate relation between the wavelength shift $\Delta\lambda_B$ of FBG and the structural strain $\varepsilon(t)$ for initial wavelengths λ_B in the range of 1520 ~1570 nm is approximately expressed as

$$\varepsilon(t) = \frac{1000\Delta\lambda_B(t)}{1.2} \tag{6}$$

where Eq. (6) can be adopted to calculate the structural strain derived from the sensing signals of FBG sensors. Previous experimental study indicates that for the surface-attached FBG sensors on the CFRP laminates or the FBG sensors embedded in the CFRP laminates, the strain transfer loss can be ignored [37]. Combined with the static calibration in Section 3.2, this supports the assumption of nearly perfect strain transfer adopted in this work. Therefore, in the laboratory tests performed at stable room temperature, the structural strain of the monitored laminates is calculated directly from the FBG wavelength shifts by using Eq. (6). The adhesive and coating layers may slightly attenuate the highest-frequency components of impact-induced signals, which is a limitation of the present study.

2.2 Fabrication of Smart CFRP and Sensor Layout

In this study, T700 unidirectional carbon fabric (Toray, Japan; 12k tow) was used as the reinforcement, and an F46 epoxy resin system served as the matrix.

The system integration of FBG sensors with the CFRP laminate comprises three key stages: (i) prepreg preparation to ensure uniform resin distribution; (ii) a controlled cure cycle to achieve optimal polymerization; and (iii) precise placement of the sensor array for monitoring structural response. As illustrated in Figs. 2 and 3, the specific steps are as follows:

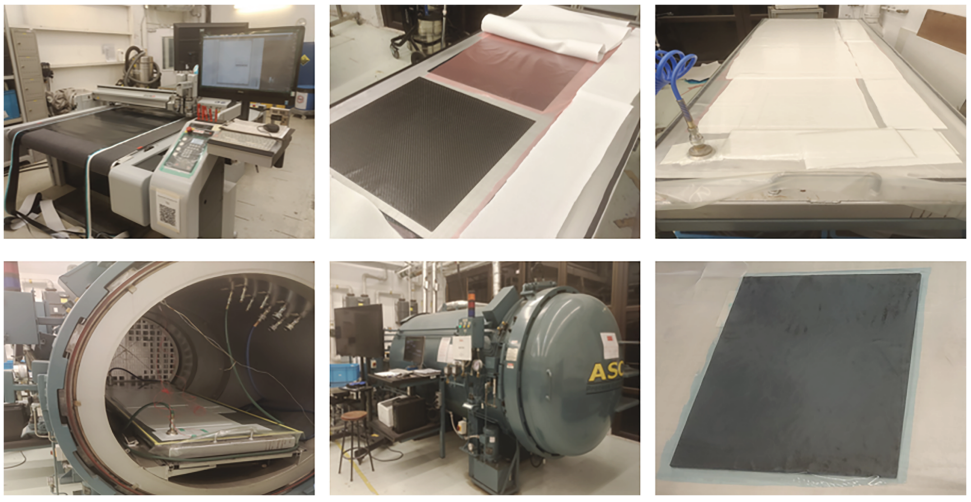

Figure 2: Physical diagram of CFRP laminate preparation

Figure 3: Items required for making the FBG sensor array: (**a**) CFRP laminates; (**b**) FBG sensors; (**c**) T-400S optical fiber fusion splicer; (**d**) SYLGARD™184 silicone elastomer

(1) Prepreg preparation

First, the unidirectional carbon fabric was cut into 450 mm × 450 mm square specimens. The epoxy matrix and curing agent were weighed to the prescribed ratio, thoroughly mixed, and then allowed to stand for degassing. During lay-up, the formulated resin was uniformly applied to both sides of the fabric using a double-sided coating method to prepare prepregs. The prepregs were stacked in an alternating cross-ply sequence with careful alignment and pre-compacted under a moderate pressure. The target laminate had nominal dimensions of 450 mm × 450 mm × 3 mm, consisting of six plies (≈0.5 mm per ply) with an orthogonal $[0/90]_3$ lay-up. The resin-wetted stack was placed into a mold, and additional resin was cast to ensure complete impregnation. The mold was then sealed to prevent resin leakage and external contamination.

(2) Curing cycle

Following prepreg preparation, the curing cycle is critical to achieving complete resin impregnation, crosslinking, and polymerization of the CFRP laminate. The process entails precise control of temperature and pressure over multiple stages. A three-stage pressure–temperature cure profile with natural cooling was adopted; after validation on small coupons, it was applied to full-scale fabrication. At the end of the final stage, heating was stopped while pressure was maintained, allowing the mold to cool naturally to room temperature to avoid internal stresses or distortion caused by rapid cooling. After reaching room temperature, the mold was opened and the cured composite part was demolded.

(3) FBG integration and layout

The smart CFRP laminate system comprised the CFRP laminate, FBG sensors fabricated from optical fiber, SYLGARD™ 184 silicone elastomer, and a T-400S fiber fusion splicer. In the present work, SYLGARD™ 184 silicone elastomer was used as the adhesive and encapsulation material. The liquid silicone was dispensed over each grating segment and then cured to form a thin, compliant strip that bonded the optical fiber to

the CFRP surface and encapsulated the FBG. This configuration is commonly adopted in surface-bonded FBG sensors to protect the fragile grating while ensuring effective strain transfer. Because only a very thin layer of this low-modulus material is used along the small grating zone, the influence on the global stiffness and impact response of the CFRP laminate is negligible, whereas the long-term durability and stability of the sensing system are improved.

Thirteen FBGs were surface-bonded to the underside of the laminate (Fig. 4). The SYLGARD™ 184 silicone elastomer mixture was adopted as the thin adhesive layer to fix the FBGs on the laminate. After curing, this layer acted as both the adhesive and protective layer of the FBG sensors. The coordinates and orientations of the sensing points are listed in Table 1. The 13 FBGs include orientations of 0°, ±45°, ±90°, and ±135°, enabling assessment of the laminate's mechanical response under static and dynamic loading. Four rectangular corner regions (10 mm × 80 mm) were clamped and held fixed, resulting in a locally clamped boundary condition at the four corners.

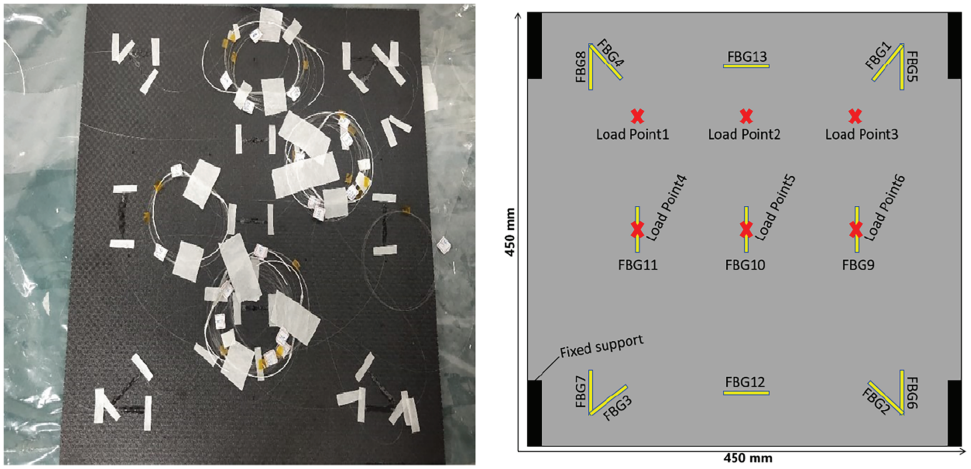

Figure 4: Schematic diagram of FBG sensor array arrangement

Table 1: Position coordinates of the installed FBG sensors

Sensors ID	x (mm)	y (mm)	Orientation (°)	Reference initial wavelength (nm)
FBG1	375	375	−135°	1542
FBG2	375	75	135°	1536
FBG3	75	75	45°	1533
FBG4	75	375	−45°	1530
FBG5	390	375	−90°	1530
FBG6	390	75	90°	1545
FBG7	60	75	90°	1542
FBG8	60	375	90°	1539
FBG9	307.5	225	90°	1536
FBG10	225	225	90°	1533
FBG11	142.5	225	90°	1530
FBG12	225	60	0°	1549
FBG13	225	390	0°	1546

3 Experimental Investigation

This section investigates the mechanical response of CFRP laminates under quasi-static and impact loading. The experimental program included static loading tests by using calibrated concentrated masses and low-velocity impact tests by using freely falling steel balls. An FBG sensor network was deployed for strain monitoring.

3.1 Experimental Setup and Protocols

Static loading: A lightweight hollow cylinder (outer diameter ≈ 15 mm, height ≈ 10 mm; negligible mass) was placed on the CFRP laminate to transmit the load, and calibrated masses of 5, 10, 15, and 20 kg were stacked on top to apply concentrated static loads at six symmetric locations (Point 1–Point 6, Fig. 4), yielding nominal forces of ~50, ~100, ~150, and ~200 N (Fig. 5a). For each location and load level, three repeats were performed. Strain signals from FBG4, FBG5, FBG9, FBG10, FBG11, and FBG13 were processed. The straight-line distances between the load points and the nearest FBG were: Point 1–FBG4, 5.30 cm; Point 2–FBG13, 5.25 cm; Point 3–FBG5, 6.45 cm; Point 4–FBG11, 3 cm; Point 5–FBG10, 0 cm; Point 6–FBG9, 3 cm.

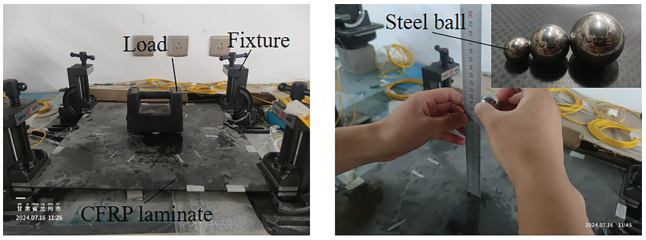

(a) Static load (b) Dynamic load

Figure 5: Physical diagram of the load application process

Dynamic loading: Low-velocity impacts were generated by freely dropping steel balls of 32.58, 110.13, and 260.93 g from heights of 10, 15, and 20 cm (Fig. 5b). Impacts were applied sequentially at Point 1–Point 6, with five repeats per condition to ensure statistical reliability; strain responses were captured by the same FBG layout as in the static tests. Load-point coordinates are listed in Table 2.

Table 2: Load application position coordinates

Item	Point 1	Point 2	Point 3	Point 4	Point 5	Point 6
x (mm)	112.5	225	337.5	112.5	225	337.5
y (mm)	337.5	337.5	337.5	225	225	225

Instrumentation: The interrogator and laptop used in the experiments are shown in Fig. 6. The interrogator sampled at 5000 Hz, while the laptop handled control, visualization, and data collection.

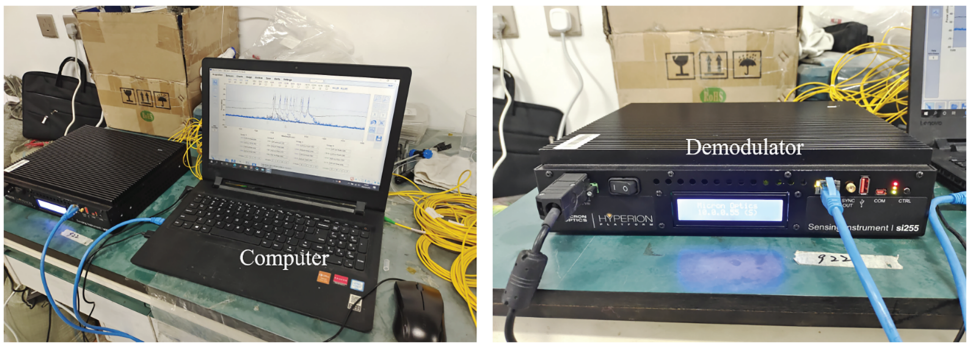

Figure 6: Experimental device

3.2 Static Response Characteristics

From the six load points in Fig. 7, the static strain response of the CFRP laminate is governed primarily by the load location, the FBG gauge orientation, and the geometric standoff to the load point. For the present loading path, gauges oriented at −45° and −90° recorded negative strain, whereas the other orientations recorded positive strain. The strain amplitude scaled approximately linearly with the applied load and decayed markedly with increasing sensor–load distance. At Point 4 and Point 6, FBG11 and FBG9 are each 3 cm from the load point and positioned nearly symmetrically; accordingly, their strain trends and magnitudes are essentially identical.

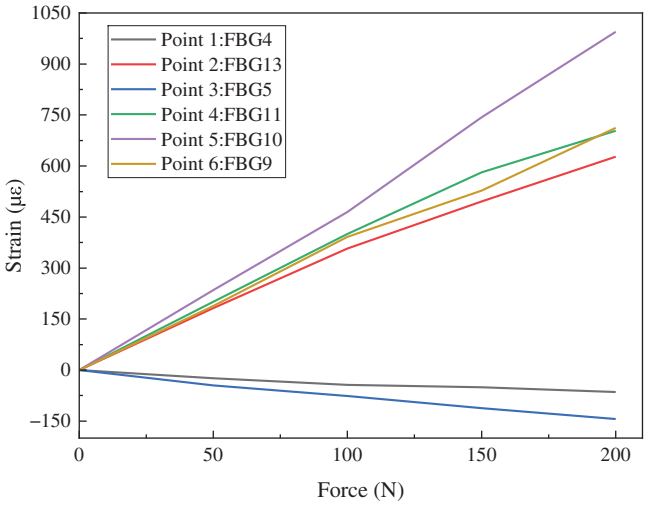

Figure 7: Strain variation of CFRP laminates under static load

As the static load was increased stepwise from 50 N to 200 N at each load point, the strains measured by all FBGs increased approximately linearly with the applied load. The small deviations observed at the highest load level are within the experimental scatter and do not show any systematic departure from linear elastic behaviour or any indication of damage.

FBG9, FBG10, and FBG11 are collinear and equally spaced (8.25 cm) with identical 90° orientation, with FBG10 centered. As shown in Fig. 8, when a 100 N static load was applied at Point 5, the three FBGs exhibited similar temporal profiles—an abrupt rise to a peak upon loading followed by gradual stabilization—while

the amplitudes differed: FBG10, being closest to the load, measured the largest strain, whereas the farther yet equidistant FBG9 and FBG11 measured smaller strains.

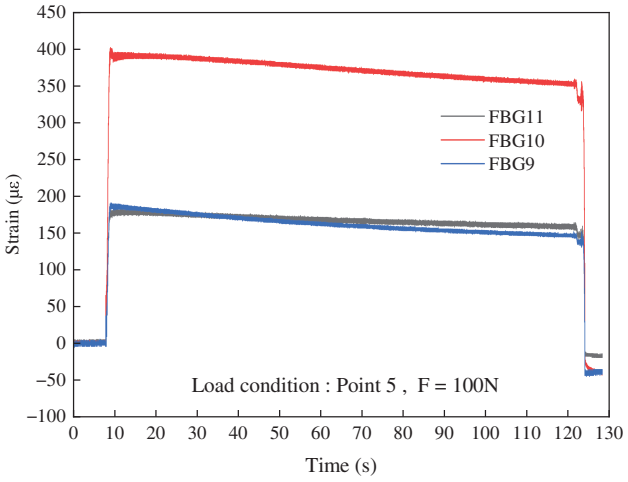

Figure 8: Comparison of strain conditions obtained by FBGs at different positions under the same force

The strain–time curves for FBG9, FBG10 and FBG11 under a nominally constant load 100 N exhibit a slightly inclined segment rather than an ideal horizontal step. This behavior is mainly attributed to slight changes in contact conditions after manual placement of the calibrated mass, together with minor time-dependent deformation of the laminate. The resulting drift is much smaller than the absolute strain level and does not affect interpretation of the static response.

These results indicate that, under the present conditions, the FBG-measured strain amplitude decays monotonically with the geometric sensor–load distance; symmetric sensors at equal distance and orientation (e.g., FBG9/FBG11) yield comparable magnitudes and waveforms, confirming the dominant role of the distance effect.

3.3 Dynamic Impact Behavior

As shown in Fig. 9a–r, the impact-induced strain is governed by the impact location relative to the FBG sensor, the sensor–impact standoff, the drop height, the steel-ball mass, and the FBG orientation. In Fig. 9a–c,g–i, the magnitude of negative strain generally exceeds that of positive strain, primarily due to the orientations of FBG4 and FBG5 at Points 1 and 3; proximity also amplifies the response, with FBG5 typically exceeding FBG4. In the remaining panels, positive strain dominates, and the distance effect persists; for example, Fig. 9m–o shows that FBG10 associated with Point 5 exhibits the largest amplitude. Overall, higher drop height or greater ball mass increases the strain response of the CFRP laminate, yielding larger FBG signal amplitudes.

The strain–time histories in Fig. 9 reflect an energy-transfer–controlled process with four stages:

- Rapid rise: an immediate jump upon wave arrival, indicating concentrated energy input;
- Peak strain: the maximum amplitude, representing local stress intensity;
- Oscillatory decay: energy dissipation due to wave reflections/interference and material damping;
- Stabilization: convergence to a residual strain or the baseline.

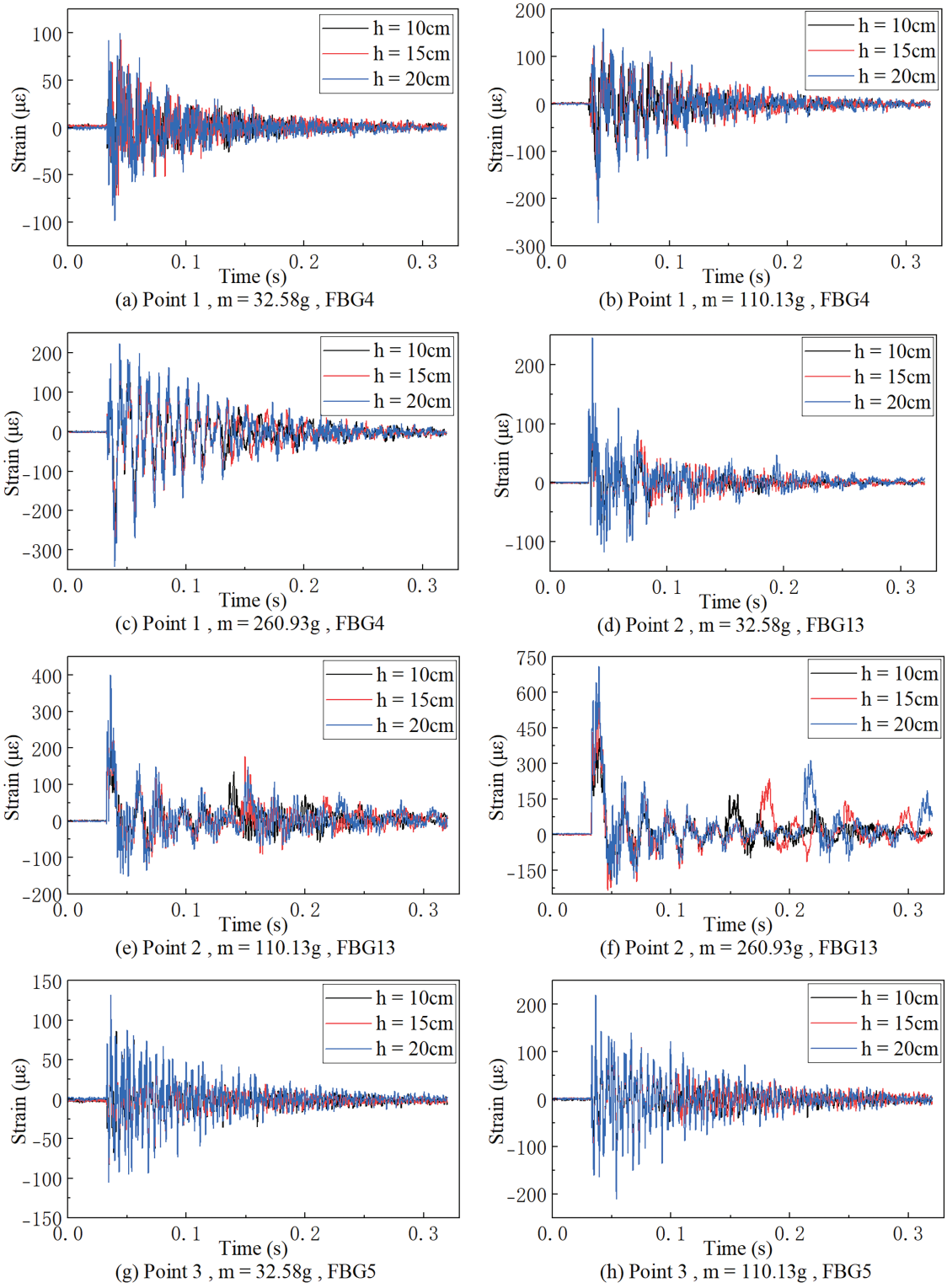

Figure 9: (Continued)

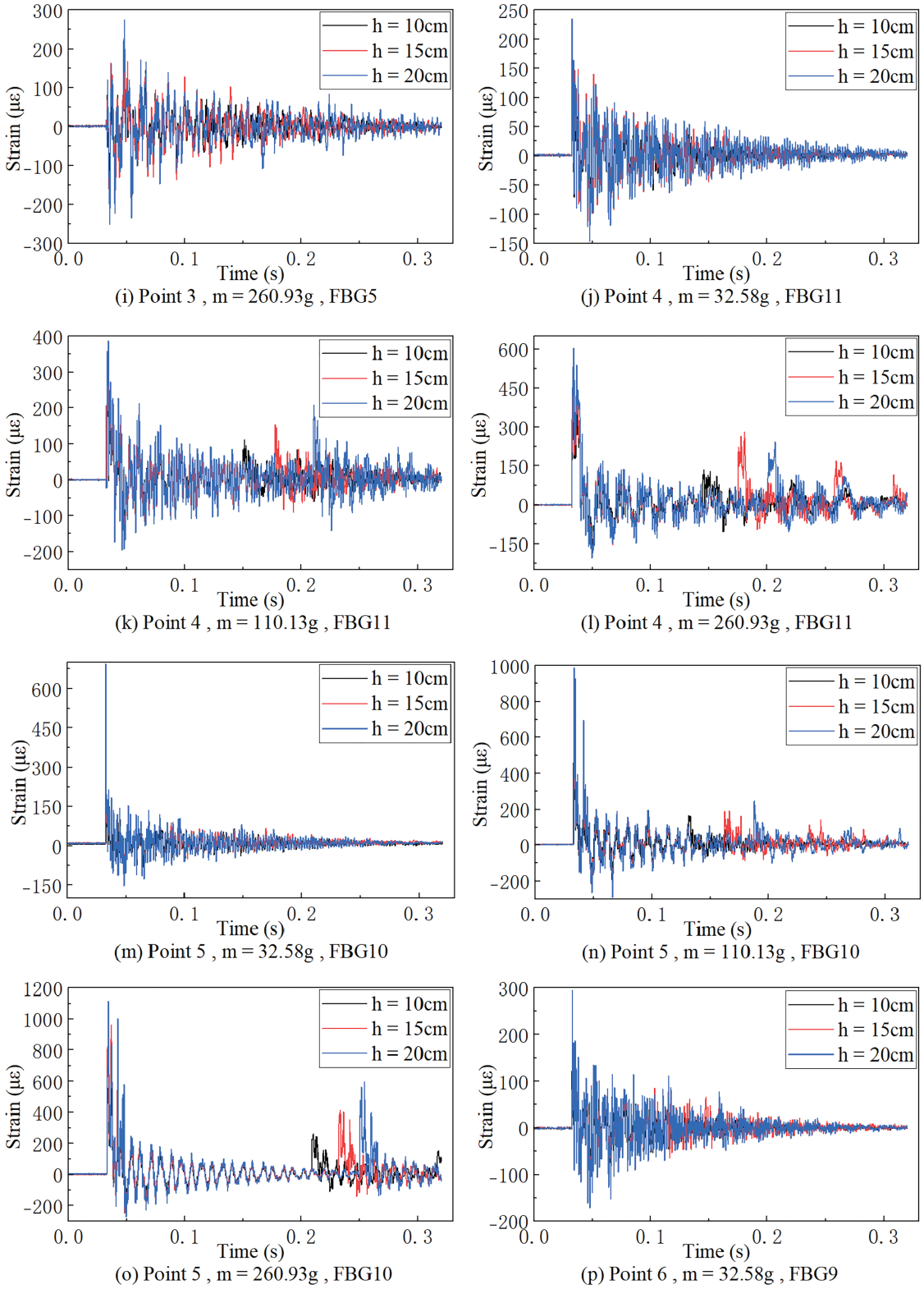

(i) Point 3 , m = 260.93g , FBG5

(j) Point 4 , m = 32.58g , FBG11

(k) Point 4 , m = 110.13g , FBG11

(l) Point 4 , m = 260.93g , FBG11

(m) Point 5 , m = 32.58g , FBG10

(n) Point 5 , m = 110.13g , FBG10

(o) Point 5 , m = 260.93g , FBG10

(p) Point 6 , m = 32.58g , FBG9

Figure 9: (Contiuned)

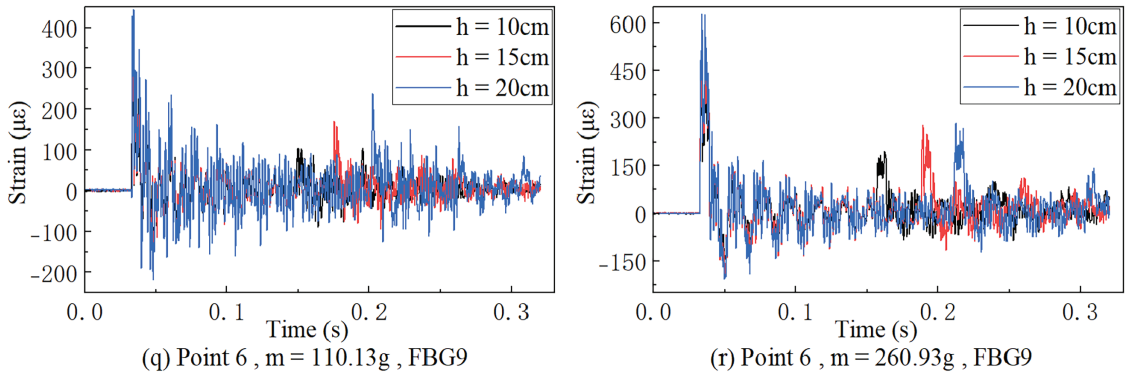

Figure 9: Strain variation in low-velocity impact experiments on CFRP laminates

Impact energy ($E = m \cdot g \cdot h$) is the primary driver of the peak strain. Using Point 5 as a case, Fig. 10 shows that, at fixed height, a heavier ball produces higher energy and thus larger strain; at fixed mass, a greater height likewise increases energy and strain.

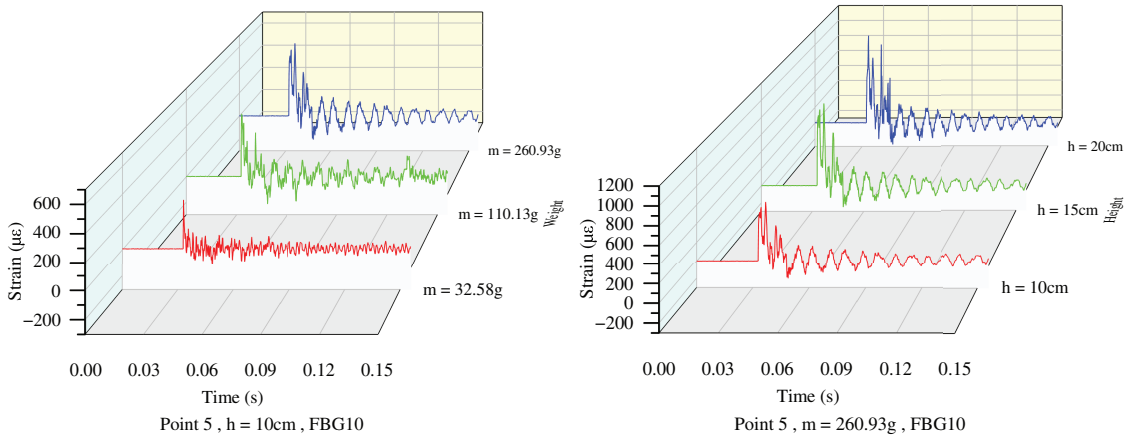

Figure 10: Effects of drop height and impactor mass on the FBG-measured response of the CFRP plate

The sensor–impact geometry strongly modulates the amplitude. Fig. 11 compares FBG9, FBG10, and FBG11 for Point 5 at 20 cm and 32.58 g: FBG10 (0 cm standoff) recorded a peak strain 2.8× that of FBG9/FBG11 (each 3 cm). The symmetry between FBG9 and FBG11 confirms positional repeatability. The attenuation follows an approximately inverse-distance relationship, consistent with the static tests but amplified by dynamic wave-propagation effects.

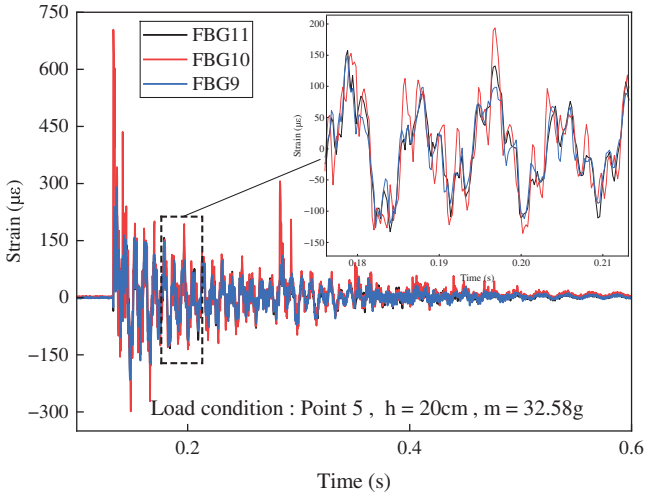

Figure 11: Comparison of the influence of FBG strain measurement distance

4 Numerical Validation and Comparative Analysis

4.1 Finite Element Simulation Model

Finite-element models of CFRP laminates incorporating surface-bonded and embedded fibers were developed in ANSYS/LS-DYNA.

4.1.1 Model Configuration of CFRP Laminates with Externally Bonded FBGs

(1) Geometry and mesh:

For the surface-bonded configuration, the CFRP laminate measures 450 mm × 450 mm × 3 mm, with six plies (0.5 mm each) and a $[0/90]_3$ layup. A shell model was generated using Mesh > Shape Mesher > 4 N SHELL, with 90 divisions along both in-plane directions, yielding 8100 shell elements.

For the embedded configuration, the FBG is located between the 3rd and 4th plies (Fig. 12). The laminate was discretized with Mesh > Shape Mesher > SOLID BOX, totaling 48,600 solid elements; the fiber was modeled with beam elements, totaling 217 beam elements.

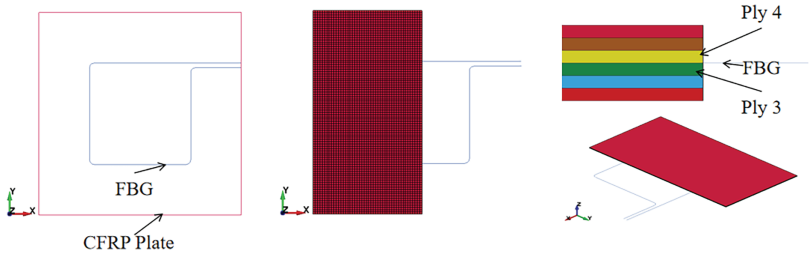

Figure 12: Mesh model of CFRP laminates with built-in optical fibers

(2) Material models:

The laminate uses material model #2 (MAT_ORTHOTROPIC_ELASTIC), and the material properties are listed in Table 3.

Table 3: Material properties of T700-12K carbon fiber/epoxy resin composite material [38]

Property	LS-DYNA value	Experimental value
Density (ton/mm^3)	RHO	1.8 × 10−9
Young's modulus—longitudinal direction (MPa)	EA	230,000
Young's modulus—transverse (in-plane) direction (MPa)	EB	40,000
Young's modulus—through-thickness (normal) direction (MPa)	EC	40,000
Poisson's ratio	PRBA	0.27
Shear modulus (MPa)	GAB	14,300
Shear modulus (MPa)	GBC	14,300
Shear modulus (MPa)	GCA	14,300
Density (ton/mm^3)	RHO	1.8 × 10−9
Young's modulus—longitudinal direction (MPa)	EA	230,000
Young's modulus—transverse (in-plane) direction (MPa)	EB	40,000

The laminate properties are identical for the embedded and surface-bonded cases. The FBG is assigned material model #1 (MAT_ELASTIC) with properties given in Table 4.

Table 4: Material properties of FBG

Property	LS-DYNA value	Experimental value
Density (ton/mm^3)	RHO	2.2×10^{-9}
Elastic modulus (MPa)	E	70 × 103
Poisson's ratio	PR	0.17

(3) Boundary conditions:

Both configurations apply identical constraints: on the top and bottom surfaces, rectangular pads (10 mm × 80 mm) at each corner were fully constrained using SPC.

4.1.2 Model Configuration of CFRP Laminates with Embedded FBGs

(1) Geometry and mesh:

For the surface-bonded configuration, the CFRP laminate mesh is identical to Fig. 12. The steel ball is modeled as a hollow sphere using solid elements generated via Mesh > Shape Mesher > SPHERE SOLID; the three ball masses match the experiment, and each ball uses 600 elements (Fig. 13).

(2) Material models:

The laminate material model is the same as in the static analysis. The steel ball is assigned material #20, MAT_RIGID, with properties listed in Table 5.

The laminate and FBG material selections follow Tables 3 and 4; the sphere material model is given in Table 5.

(3) Boundary conditions:

Both the surface-bonded and embedded FBG models apply locally clamped constraints along all four edges, consistent with the experiment.

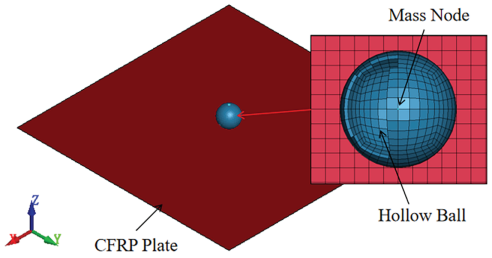

Figure 13: Impact model

Table 5: Material properties of the steel ball [39]

Property	LS-DYNA value	Experimental value
Density (ton/mm^3)	RHO	7.85×10^{-9}
Young's modulus (MPa)	E	210×10^3
Poisson's ratio	PR	0.3

4.2 Results Analysis

4.2.1 Static Load Response Analysis

Based on the FE results for Points 1–6, the CFRP laminate exhibits pronounced orthotropic anisotropy and layerwise behavior under static loading. The typical patterns are as follows. Under concentrated loads of 50–200 N, the stress–strain response is consistent across cases. For the in-plane stresses (X/Y; Fig. 14), the maxima occur near the constrained corners (e.g., the upper-left corner for Point 1), and the amplitudes scale approximately linearly with the applied load.

As shown in Figs. 15 and 16, at various FBG locations the through-thickness stress displays a nonlinear gradient under concentrated loading: amplitudes in both X and Y increase toward the loaded surface and decay approximately exponentially with depth. Within a given ply level, stress magnitudes differ across FBG positions, indicating that load-transfer paths are jointly governed by local geometry and boundary constraints. The Y-direction response is generally more sensitive than the X-direction, implying a dominant role of transverse in-plane deformation.

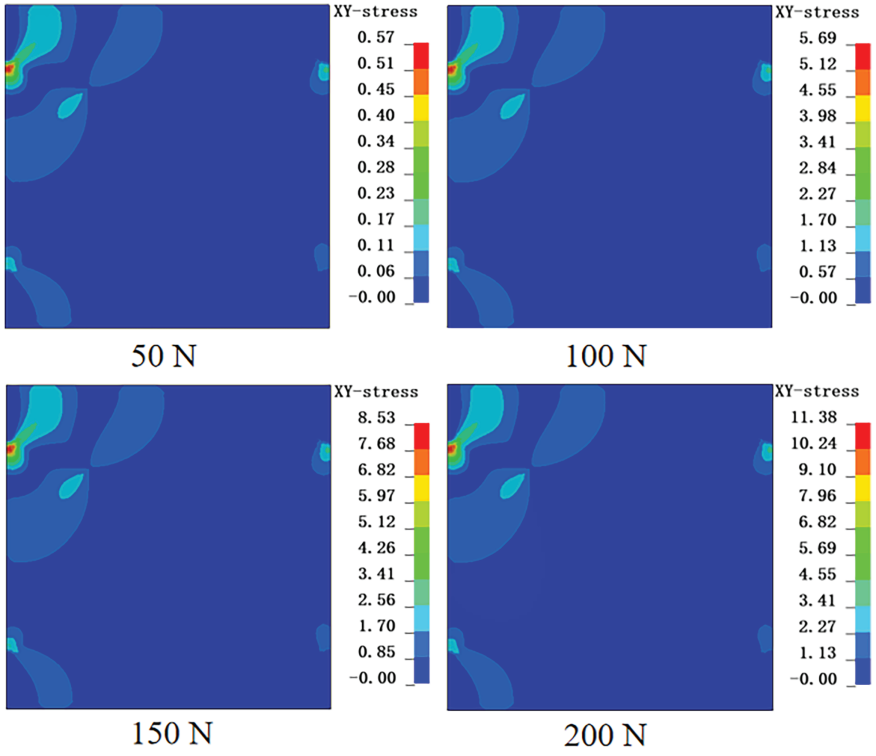

Figure 14: Stress nephogram in the *XY* direction under the action of a concentrated force

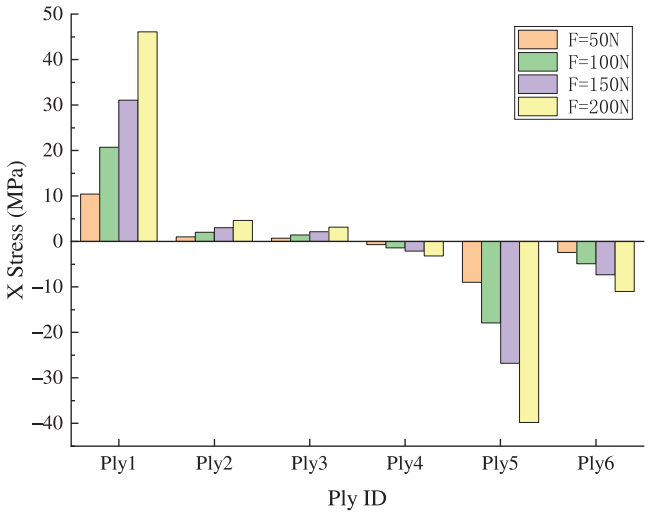

Figure 15: The stress variation in the *X* direction of each layer element at the FBG13 position under the action of a concentrated force

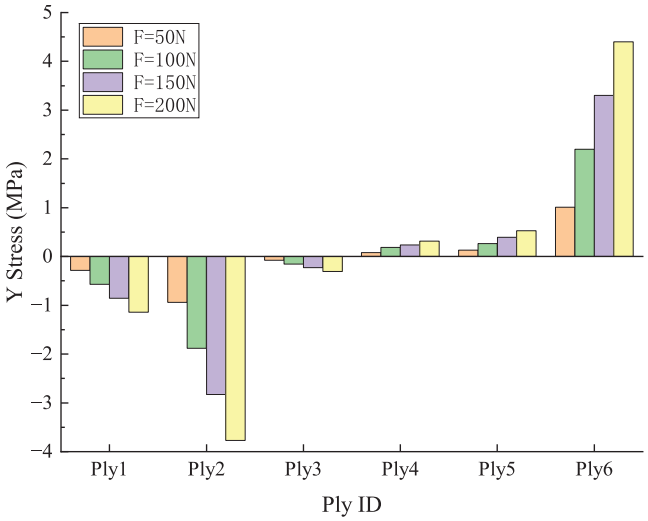

Figure 16: The stress variation in the *Y* direction of each layer element at the FBG5 position under the action of a concentrated force

The strain contours at 200 N (Fig. 17) reveal interlaminar asymmetry: in Layers 1–3, tensile strain peaks near the constraints while compression appears at the load point; Layers 4–6 exhibit the opposite pattern. The layers thus form a mirror distribution—compression/tension on opposite sides—consistent with bending about a neutral plane.

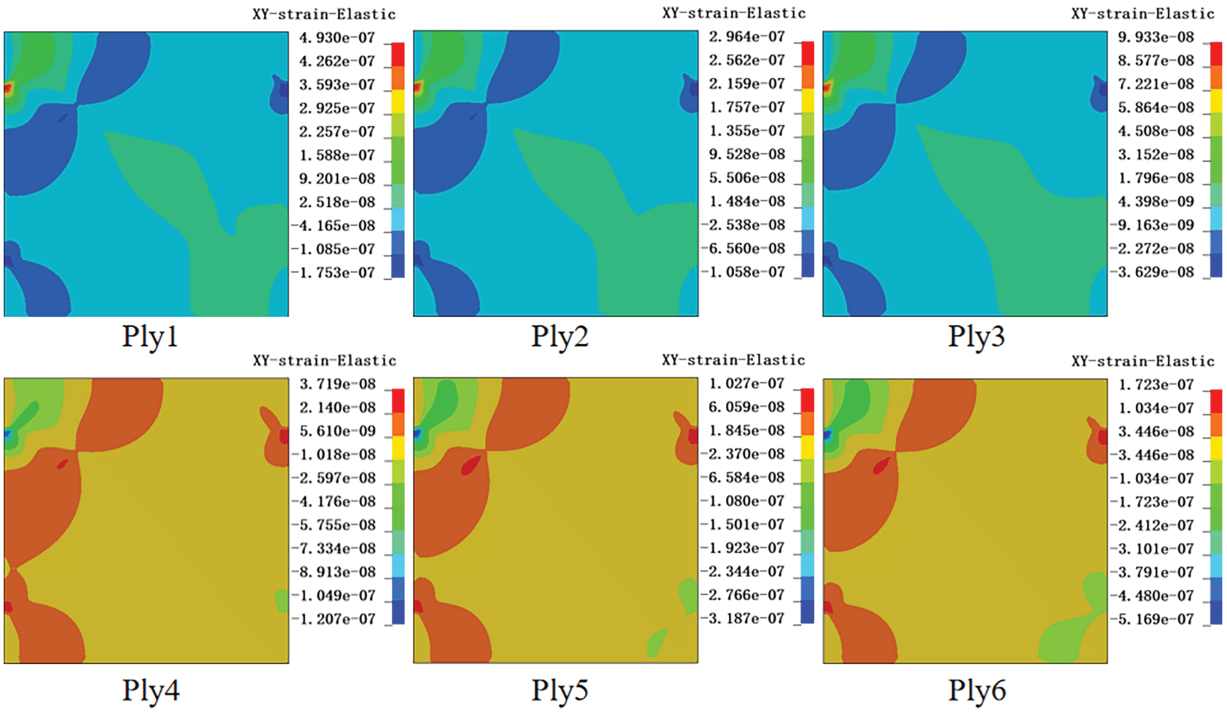

Figure 17: Strain nephogram in the *XY* direction of each layer under a concentrated force of 200 N

Out-of-plane displacement increases nearly linearly with load (Table 6); the central load point shows the largest deflection (Point 5: 1.9667 mm at 200 N).

Table 6: Vertical displacement under the action of a concentrated force

Items	Point 1	Point 2	Point 3	Point 4	Point 5	Point 6
F = 50 N	0.2834	0.45	0.2834	0.3689	0.4917	0.3689
F = 100 N	0.5669	0.9	0.5669	0.7378	0.9833	0.7378
F = 150 N	0.8503	1.35	0.8503	1.1067	1.475	1.1067
F = 200 N	1.1337	1.8	1.1337	1.4755	1.9667	1.4755

Embedded fibers (diameters 0.125 and 0.250 mm) introduce negligible perturbation to the global structure under static loads up to 1000 N. The equivalent-stress field in the CFRP matches the fiber-free case (Fig. 18), with peak stress localized near the constraints (426.07 MPa at 1000 N). Around the fibers at (337.5, 337.5) and (225, 225), local stress variations are minimal and shape-consistent, with no abnormal spikes.

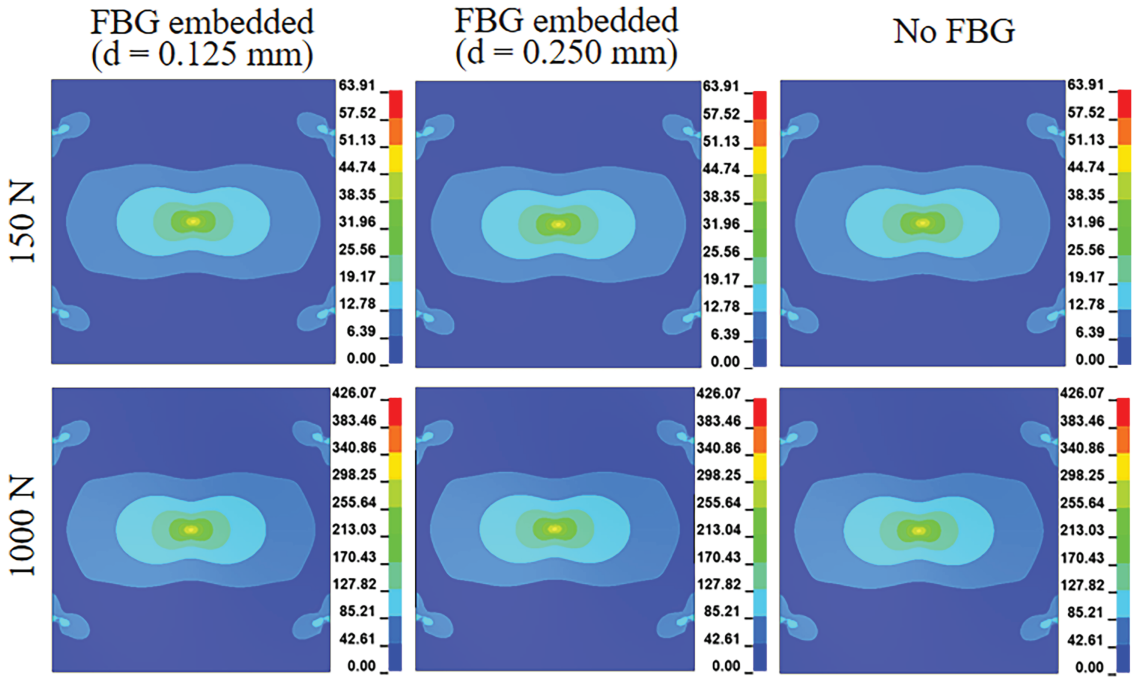

Figure 18: Equivalent stress nephograms under concentrated forces of 150 and 1000 N

Stresses of the optical fiber embedded in CFRP laminates increase with both the load and the diameter of the fiber, as shown in Fig. 19. At 1000 N, the max stress of the optical fiber with diameter of 0.250 mm reaches 155.67 MPa.

The displacement difference between embedded and non-embedded models is ≤0.0001% (Table 7), confirming invariance of the global response.

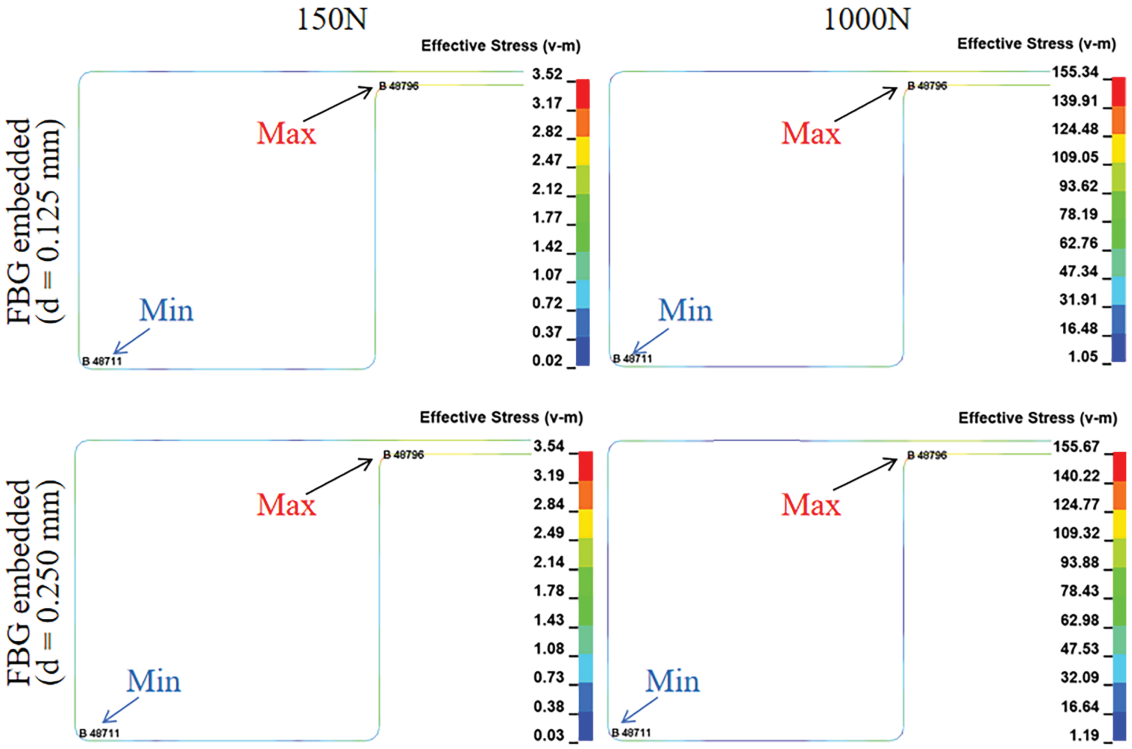

Figure 19: Nephogram of stress variation of optical fibers under concentrated forces of 150 and 1000 N

Table 7: Displacement comparison

Items	150 N	1000 N
No FBG embedded (mm)	1.43329	9.55527
d = 0.125 mm FBG embedded (mm)	1.43329	9.55526
d = 0.250 mm FBG embedded (mm)	1.43329	9.55527
Differences (%)	0	1.0465e−4

The simulated strain trend for the surface-bonded FBG agrees closely with the experiment (Fig. 20), validating the finite element model (FEM) approach. This agreement also indicates that the thin adhesive layer and fiber coating do not significantly distort the measured strain histories in the frequency range.

In summary, for concentrated loads of 50–1000 N, the laminate exhibits stable stress concentration near the constraints with peak values growing approximately linearly with load; through-thickness stress decays roughly exponentially from the compressed surface toward the neutral plane, with higher sensitivity in the Y direction than in X. Under identical boundary and discretization conditions, embedded fibers (d = 0.125/0.25 mm) have negligible influence on global stiffness and equivalent fields (displacement difference <0.0001%), while the fiber stress itself increases with load and diameter; for the surface-bonded case, simulation and measured strain trends are consistent.

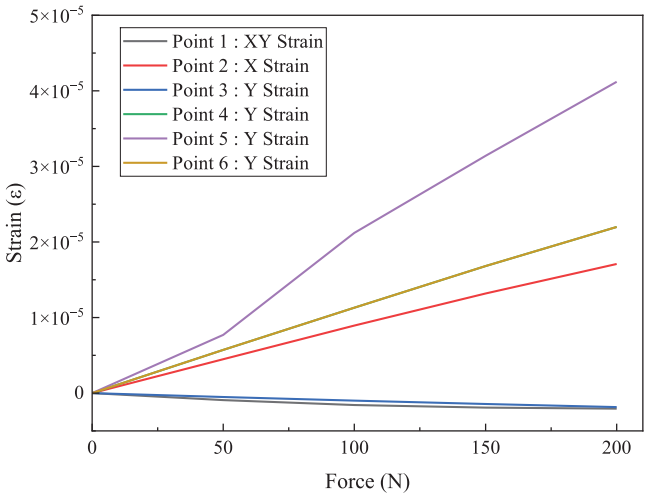

Figure 20: The strain changes at the positions corresponding to FBG measuring points from Point 1 to Point 6

4.2.2 Impact Dynamics Analysis

Because of directional differences in elastic moduli ($E_A > E_B$), stress propagation in the CFRP laminate exhibits pronounced orthotropy. As shown in Fig. 21, at the same time step a heavier ball (e.g., 260.93 g) amplifies the local stress amplitude compared with lighter balls (32.58, 110.13 g). Fig. 22 further indicates that wave speed along the fiber direction (E_A) exceeds that in the transverse direction (E_B), owing to the higher modulus of E_A.

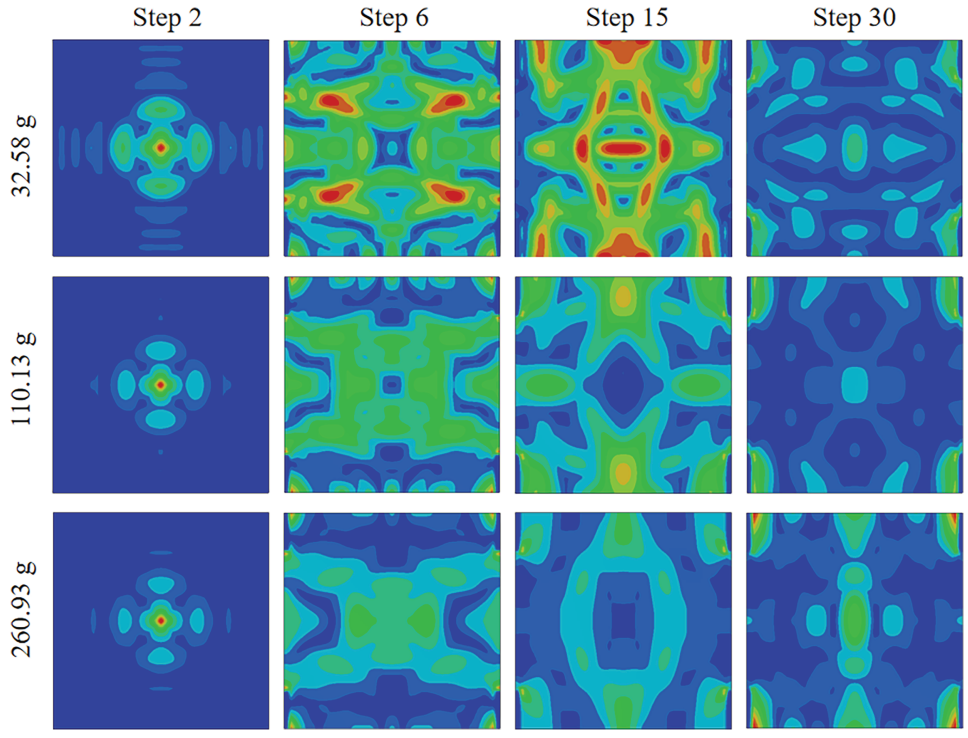

Figure 21: Strain nephograms of CFRP laminates under impact by steel balls of three different masses

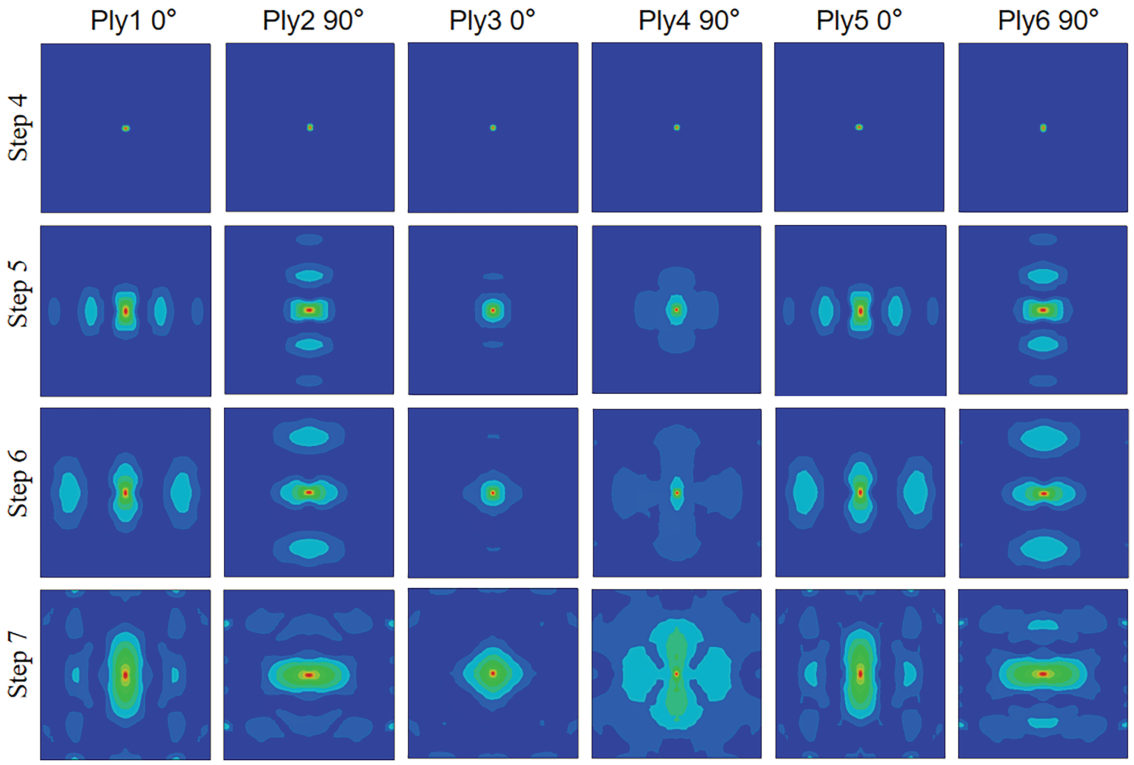

Figure 22: Stress propagation diagram of CFRP laminates under impact load of 260.93 g steel balls

For the Point 5 (225, 225) impact, notable stress concentrations occur in Layers 2 and 6, with peak stresses of 111.04 and 123.33 MPa, respectively (Fig. 23). Responses in other layers are smaller, consistent with the FBG measurements.

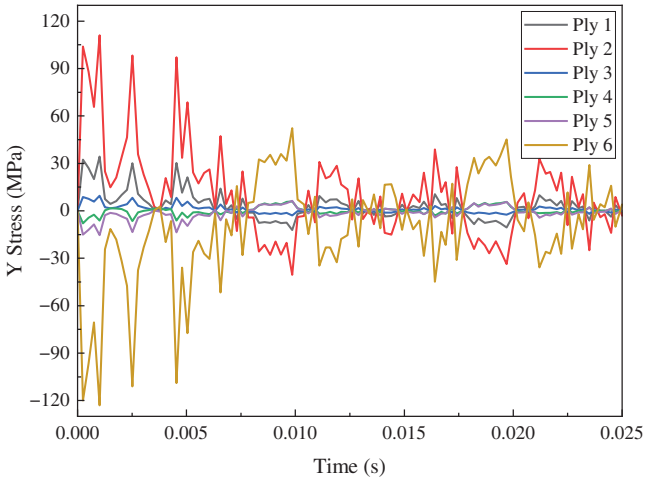

Figure 23: The *Y*-direction stress variation of each layer element at Point 5 (225, 225)

The contact peak force increases monotonically with the impactor mass, matching the experimental trend: the 260.93 g ball yields 522.85 N, exceeding 495.23 N (110.13 g) and 371.11 N (32.58 g). The section resultant force and energy likewise rise with mass and track the contact-force amplitude: 3155.2 N for

260.93 g, vs. 1084.9 and 220.96 N for 110.13 and 32.58 g. The absorbed kinetic energy spans 65.18–521.93 N·mm. Elastic rebound causes oscillatory fluctuations in the energy histories, yet the system energy error remains within 10% for all cases (Fig. 24). Similar trends in absorbed energy and damage mechanisms for hybrid metal–composite laminates have been reported by Khan et al. [40], which provides a useful reference for interpreting the present energy histories.

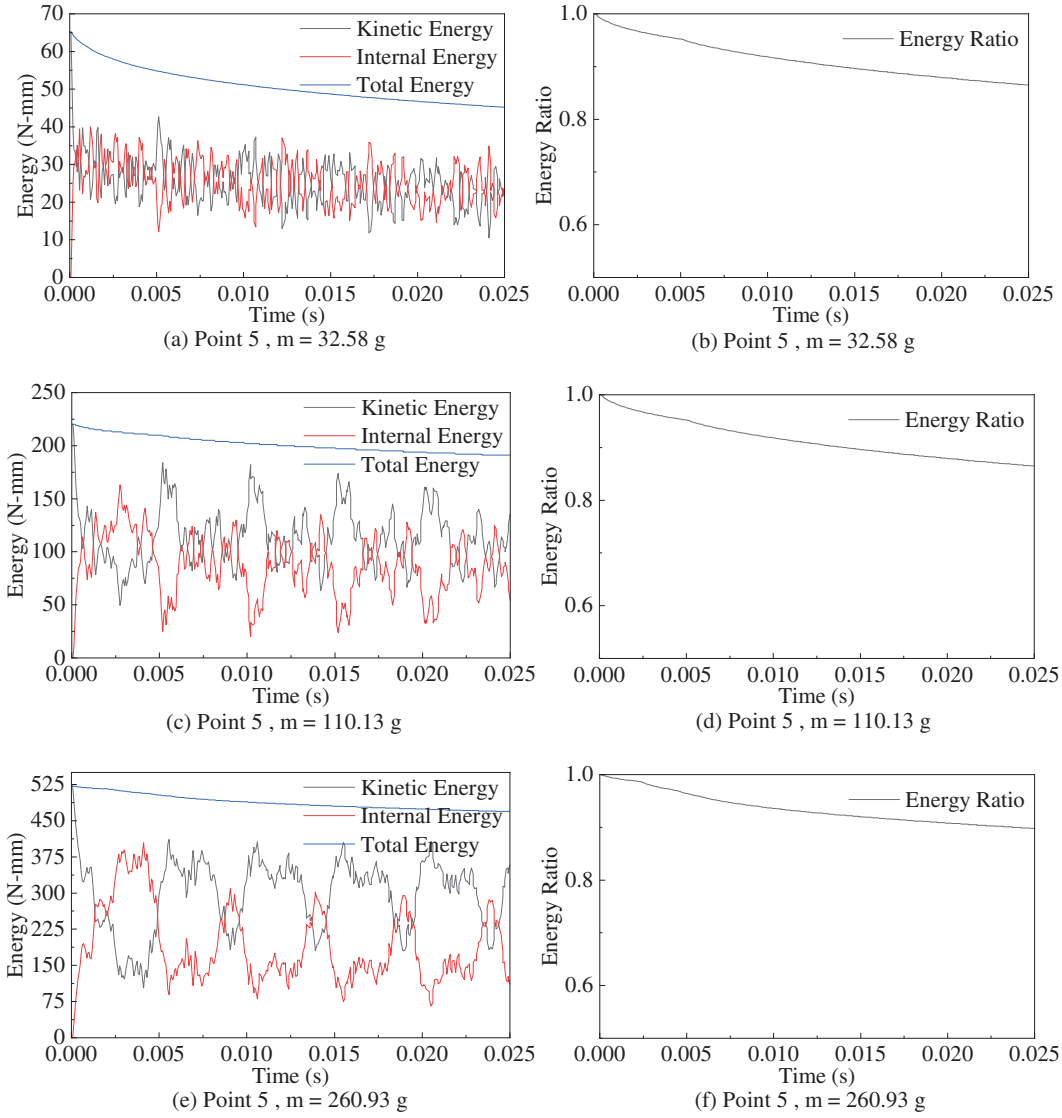

Figure 24: System energy change of CFRP laminates under steel ball impact

An FBG embedded at the 3–4 ply interface (diameters 0.125, 0.250 mm) induces a slight stress redistribution (Fig. 25). The global stress contours remain essentially unchanged relative to the fiber-free laminate (Fig. 26), but a subtle interlaminar effect appears at (337.5, 337.5 mm) (Table 8):

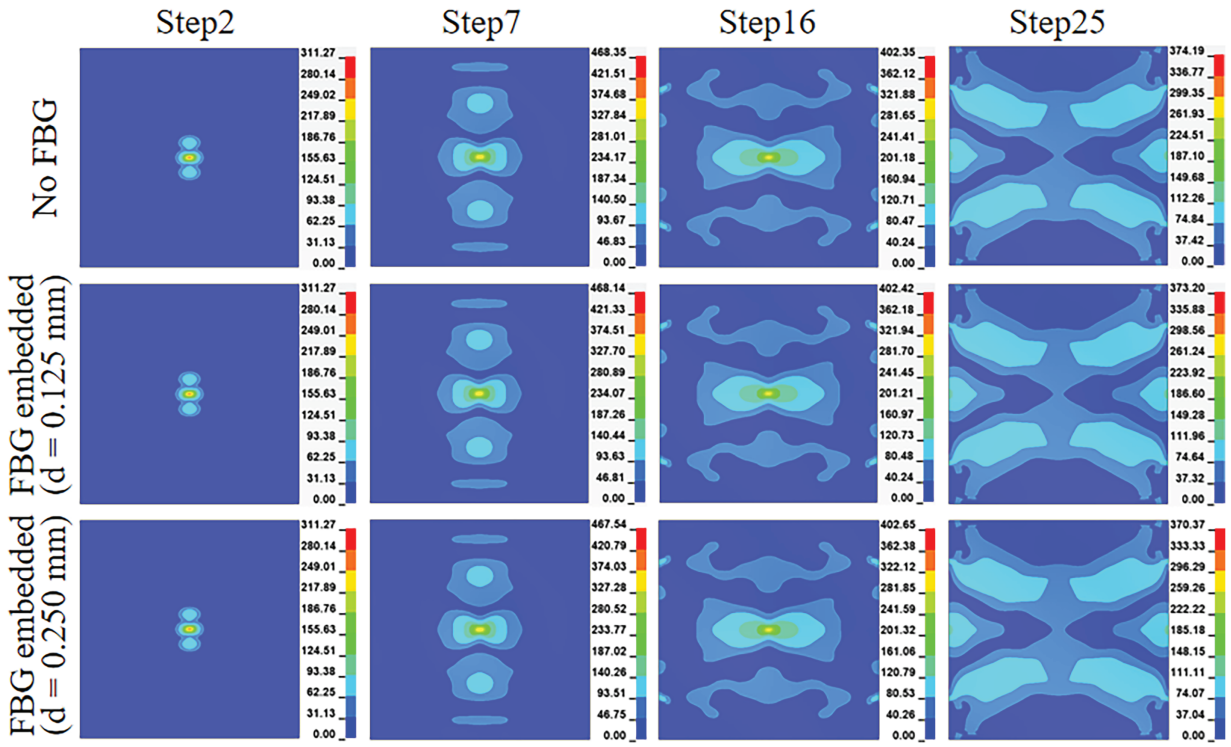

Figure 25: Comparison of stress nephograms of CFRP laminates under impact load

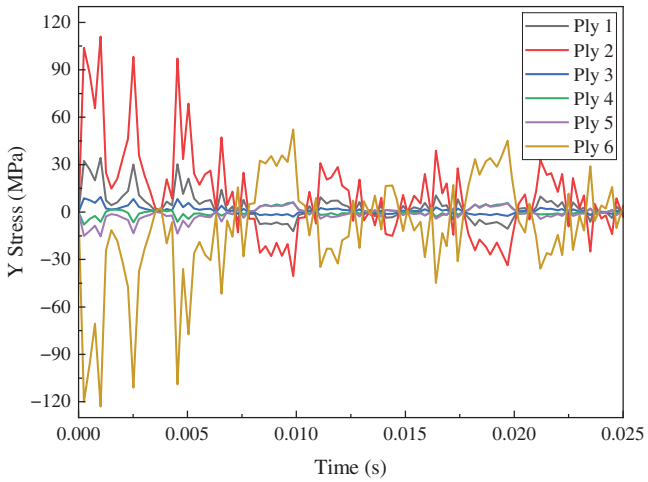

Figure 26: Comparison of stresses in the elements at position (337.5, 337.5) in the 3rd and 4th layers of the CFRP laminate

Table 8: Comparison of the maximum and minimum stresses of the elements at position (337.5, 337.5 mm) in the 3rd and 4th layers

Ply ID	Types	No FBG (MPa)	0.125 mm FBG (MPa)	0.250 mm FBG (MPa)
Ply 3	Max	7.5001	7.5036	7.5037
	Min	−3.7534	−3.7460	−3.7242
Ply 4	Max	5.8287	5.7905	5.6827
	Min	−7.8642	−7.8288	−7.7389

Layer 3: peak stress increases by 0.0474% (0.125 mm) and 0.0480% (0.250 mm);

Layer 4: peak stress decreases by 0.66% (0.125 mm) and 2.51% (0.250 mm), while the minimum increases by 0.4527% and 1.6191%.

The total system energy is identical across configurations (7829.35 N·mm). After 0.00122 s, kinetic-energy curves diverge slightly, with larger FBG diameter yielding marginally lower kinetic energy. The energy error remains ≤10%, confirming model validity; embedded FBGs introduce only minor peak differences without altering the overall energy evolution. The effect on contact peak force is <3%, with highly consistent time histories. Specifically (Figs. 27 and 28), embedding reduces the contact peak force by 0.576% (0.125 mm) and 2.345% (0.250 mm), and the section resultant force by 0.118% and 0.488%, respectively.

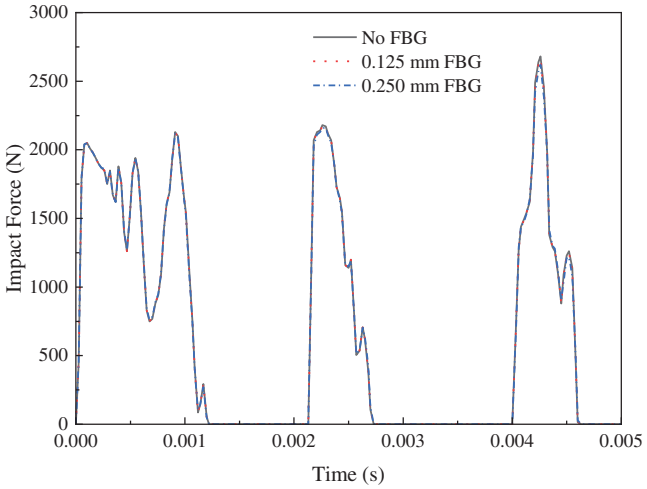

Figure 27: Force situation of CFRP laminates with embedded optical fibers

For all impact simulations, both the CFRP laminate and the embedded optical fiber were modeled as linear-elastic materials without matrix cracking, fiber breakage, delamination, or debonding at the fiber–matrix interface. Consequently, the present model characterizes the non-damaging response regime and cannot directly predict impact-induced failure or progressive damage. Under higher-energy impacts that trigger damage, an embedded fiber may act as a local stress raiser and modify crack initiation and growth. Capturing such effects would require progressive-damage and cohesive-zone modeling. Extending the present framework in this direction is an important topic for future work.

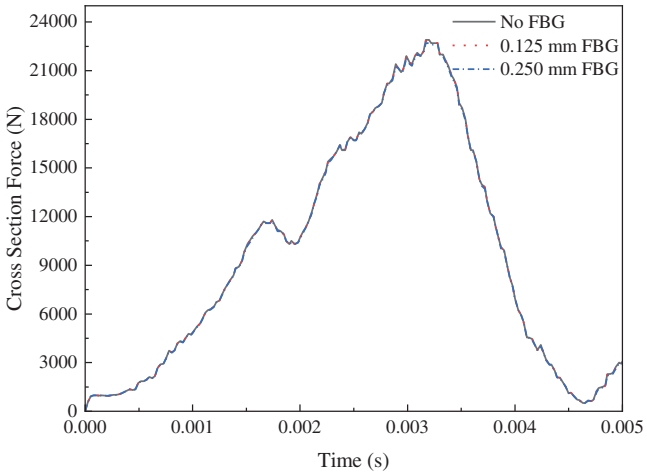

Figure 28: Resultant force situation of the cross-section of CFRP laminates with embedded optical fibers

Within a linear-elastic framework and unified modeling parameters, the CFRP laminate shows strongly orthotropic wave propagation, and increased mass amplifies local stress, contact peak force, and section resultant force (numerical trends agree with the tests, with energy error <10%). Embedded FBGs cause only <2.6% local adjustments of internal stress, <0.5% change in local resultant force, and a modest attenuation of the contact peak force by 0.6% (d = 0.125 mm) to 2.3% (d = 0.25 mm), while the waveform morphology remains consistent. Therefore, within the present non-damaging impact regime, embedded FBGs are predicted to have only a small influence on the global impact response, but to slightly modify the local stress state in the neighboring plies. From a durability perspective, it is nevertheless recommended to embed coated fibers so that the sensing element can survive the full service life of the laminate. The quantified changes, on the order of a few percent in peak force and less than 3% in local stress, indicate that small compensation factors could be considered in engineering practice. These results should, however, be interpreted as numerical predictions pending experimental verification.

5 Conclusions

This paper presents a systematic study on the response mechanisms and impact resistance of smart CFRP laminates with embedded/surface-bonded FBG sensors under combined static and dynamic loads, A complete technical framework is established, covering fabrication process, mechanical experiments, multi-scale finite element modeling and validation. A quantitative comparison of the two FBG integration strategies is conducted from the dual dimensions of mechanical performance and SHM effectiveness. The main conclusions are as follows:

(1) Under static loading, the strain-load relationship is approximately linear; the strain amplitude decays monotonically with distance and exhibits significant directionality. Under impact, the strain response shows a four-stage characteristic of rapid rise—peak—decay—stabilization. Within the energy range of this experiment, the peak strain is monotonically positively correlated with the impact energy.

(2) Under consistent boundary and discretization settings, the finite element results are generally consistent with experiments and reproduce the orthotropic propagation characteristics. Within this linear-elastic framework, embedded FBGs are predicted to have only a small influence on the overall displacement field and energy evolution, while causing a slight decrease (<3%) in the peak impact force.

(3) Validated by numerical simulation, the surface-bonded method facilitates deployment and replacement. The embedded method has a limited impact on the overall response under linear-elastic assumptions, but causes a slight attenuation of the peak (0.6%–2.3%). These quantitative results can provide reference for the trade-off between load-bearing performance and monitoring performance.

The main research findings regarding embedded FBG were obtained through LS-DYNA finite element simulation, and corresponding impact experiments with embedded fibers were not conducted in this study. The simulation results are therefore relatively idealized and may differ from the actual behavior, especially when damage initiates. Subsequent research will implement dedicated low-velocity impact tests on laminates with embedded FBGs to validate and refine these numerical predictions, and will incorporate progressive-damage modeling to investigate the effect of embedded fibers on damage initiation and evolution. In future work, the performance evaluation of smart CFRP plate structures can be further enhanced by physical model analysis integrated with massive data and machine learning algorithms to achieve rapid inversion and prediction of impact location–energy–damage level.

Acknowledgement: Special thanks are due to Prof. Jinping Ou and Prof. Zhi Zhou of Dalian University of Technology, and Prof. Youhe Zhou and Prof. Xingzhe Wang of Lanzhou University. The findings and opinions expressed in this article are only those of the authors and do not necessarily reflect the views of the sponsors.

Funding Statement: The work was supported by the Fundamental Research Funds for the Central Universities (lzujbky-2024-05); Industrial Support Plan Project of Provincial Education Department of Gansu (2025CYZC-003 and CYZC-2024-10); Innovation Foundation of Provincial Education Department of Gansu (2024B-005); Scientific Department of Gansu (18YF1GA096, 24CXGA083, 24CXGA024, JK2024-28, JK2024-32, 23CXJA0007).

Author Contributions: You-Yong Tang: data curation, writing—original draft preparation; Yong-Hao Liu and Dong-Yang Wei: experimental analysis, formal analysis; Xiao-Wei Feng: project administration, investigation; Jose Campos e Matos and David Hui: supervision, investigation; Hua-Ping Wang: methodology, writing—review and editing. All authors reviewed and approved the final version of the manuscript.

Availability of Data and Materials: The data that support the findings of this study are available from the corresponding author upon reasonable request.

Ethics Approval: Not applicable.

Conflicts of Interest: The authors declare no conflicts of interest.

References

1. Vijayan DS, Sivasuriyan A, Devarajan P, Stefańska A, Wodzyński Ł, Koda E. Carbon fibre-reinforced polymer (CFRP) composites in civil engineering application—a comprehensive review. Buildings. 2023;13(6):1509. doi:10.3390/buildings13061509.
2. Zhang J, Lin G, Vaidya U, Wang H. Past, present and future prospective of global carbon fibre composite developments and applications. Compos Part B Eng. 2023;250(5077):110463. doi:10.1016/j.compositesb.2022.110463.
3. Chen C, Wang HP, He SZ, Chen J, Sun L. Random vibration and fatigue performance analysis of carbon-fiber composite antenna beams based on fiber-Bragg-grating sensor arrays. Chin J Appl Mech. https://link.cnki.net/urlid/61.1112.O3.20250106.1413.024. (In Chinese).
4. Lai J, Yu Y, Zhang X, Qiang W, Zhang X. Interlaminar fracture toughness and impact resistance of carbon fiber reinforced composite with magnetic aligned CNTs. Compos Part B Eng. 2025;291(2):112008. doi:10.1016/j.compositesb.2024.112008.

5. Mohammad Fikry MJ, Arai Y, Inoue R, Vinogradov V, Tan KT, Ogihara S. Damage behavior in unidirectional CFRP laminates with ply discontinuity. Appl Compos Mater. 2025;32(4):1481–99. doi:10.1007/s10443-025-10320-w.
6. Liu Y, Huang K, Wang ZX, Li Z, Chen L, Shi Q, et al. Cross-scale data-based damage identification of CFRP laminates using acoustic emission and deep learning. Eng Fract Mech. 2023;294:109724. doi:10.1016/j.engfracmech.2023.109724.
7. Zhang X, Wu X, He Y, Yang S, Chen S, Zhang S, et al. CFRP barely visible impact damage inspection based on an ultrasound wave distortion indicator. Compos Part B Eng. 2019;168(3):152–8. doi:10.1016/j.compositesb.2018.12.092.
8. Munoz V, Valès B, Perrin M, Pastor ML, Welemane H, Cantarel A, et al. Damage detection in CFRP by coupling acoustic emission and infrared thermography. Compos Part B Eng. 2016;85(3):68–75. doi:10.1016/j.compositesb.2015.09.011.
9. Shen FK, Wang SK, Zhang JY, Xia ZG, Peng BR, Sasy Chan YW, et al. FBG monitoring information-motivated anti-fatigue performance analysis of CFRP composites based on non-destructive tests. Polymers. 2025;17(13):1817. doi:10.3390/polym17131817.
10. Jayawickrema UMN, Herath HMCM, Hettiarachchi NK, Sooriyaarachchi HP, Epaarachchi JA. Fibre-optic sensor and deep learning-based structural health monitoring systems for civil structures: a review. Measurement. 2022;199(3):111543. doi:10.1016/j.measurement.2022.111543.
11. Okagawa S, Bernus P, Noran O. Realtime health monitoring of composite structures using FBG sensors. IFAC-PapersOnLine. 2022;55(19):157–62. doi:10.1016/j.ifacol.2022.09.200.
12. Güemes A, Fernandez-Lopez A, Pozo AR, Sierra-Pérez J. Structural health monitoring for advanced composite structures: a review. J Compos Sci. 2020;4(1):13. doi:10.3390/jcs4010013.
13. Lopes C, Araújo A, Silva F, Pappas PN, Termine S, Trompeta AA, et al. Smart carbon fiber-reinforced polymer composites for damage sensing and on-line structural health monitoring applications. Polymers. 2024;16(19):2698. doi:10.3390/polym16192698.
14. Wang HP, Dai JG, Wang XZ. Improved temperature compensation of fiber Bragg grating-based sensors applied to structures under different loading conditions. Opt Fiber Technol. 2021;63(5):102506. doi:10.1016/j.yofte.2021.102506.
15. Cheng WZ. Flight test technique for helicopter blade strain measurements based on fiber Bragg grating. Chin J Appl Mech. 2016;33(3):466–71. (In Chinese). doi:10.11776/cjam33.03.D085.
16. Zhang C, Lai SX, Wang HP. Structural modal parameter recognition and related damage identification methods under environmental excitations: a review. Struct Durab Health Monit. 2025;19(1):25–54. doi:10.32604/sdhm.2024.053662.
17. Zou R, Tong Y, Liu J, Sun J, Xian D, Tang Q. Progress of proximity sensors for potential applications in electronic skins. Trans Tianjin Univ. 2024;30(1):40–62. doi:10.1007/s12209-023-00379-6.
18. Yashiro S, Okabe T, Takeda N. Damage identification in a holed CFRP laminate using a chirped fiber Bragg grating sensor. Compos Sci Technol. 2007;67(2):286–95. doi:10.1016/j.compscitech.2006.08.004.
19. Wang H, Dai JG. Strain transfer analysis of fiber Bragg grating sensor assembled composite structures subjected to thermal loading. Compos Part B Eng. 2019;162(4):303–13. doi:10.1016/j.compositesb.2018.11.013.
20. Yashiro S, Takeda N, Okabe T, Sekine H. A new approach to predicting multiple damage states in composite laminates with embedded FBG sensors. Compos Sci Technol. 2005;65(3–4):659–67. doi:10.1016/j.compscitech.2004.09.022.
21. Liu RM, Liang DK. Test attempt to shear strength of interface for embedded optical fiber sensors. Chin J Appl Mech. 2009;26(4):820–3+844. (In Chinese).
22. Lu S, Jiang M, Sui Q, Sai Y, Jia L. Damage identification system of CFRP using fiber Bragg grating sensors. Compos Struct. 2015;125(7):400–6. doi:10.1016/j.compstruct.2015.02.038.
23. Geng X, Jiang M, Gao L, Wang Q, Jia Y, Sui Q, et al. Sensing characteristics of FBG sensor embedded in CFRP laminate. Measurement. 2017;98(13a):199–204. doi:10.1016/j.measurement.2016.12.003.

24. Zhu P, Xie X, Sun X, Soto MA. Distributed modular temperature-strain sensor based on optical fiber embedded in laminated composites. Compos Part B Eng. 2019;168(15):267–73. doi:10.1016/j.compositesb.2018.12.078.
25. Rocha H, Lafont U, Nunes JP. Optimisation of through-thickness embedding location of fibre Bragg grating sensor in CFRP for impact damage detection. Polymers. 2021;13(18):3078. doi:10.3390/polym13183078.
26. Dong ZJ, Li SL, Wen JY, Leng Z. Real-time temperature field measurement of asphalt pavement based on fiber Bragg grating measuring technology. J Traffic Transp Eng. 2014;14(2):1–6+13. (In Chinese). doi:10.3969/j.issn.1671-1637.2014.02.002.
27. Kinet D, Mégret P, Goossen KW, Qiu L, Heider D, Caucheteur C. Fiber Bragg grating sensors toward structural health monitoring in composite materials: challenges and solutions. Sensors. 2014;14(4):7394–419. doi:10.3390/s140407394.
28. Zhu P, Feng X, Liu Z, Huang M, Xie H, Soto MA. Reliable packaging of optical fiber Bragg grating sensors for carbon fiber composite wind turbine blades. Compos Sci Technol. 2021;213(1):108933. doi:10.1016/j.compscitech.2021.108933.
29. Giannaros E, Kotzakolios A, Kostopoulos V, Campoli G. Hypervelocity impact response of CFRP laminates using smoothed particle hydrodynamics method: implementation and validation. Int J Impact Eng. 2019;123:56–69. doi:10.1016/j.ijimpeng.2018.09.016.
30. Liu T, Xu X, Chen L, Kim S, Hong S. Numerical analysis on dynamic response of CFRP-wrapped RC columns under lateral impact loading. Materials. 2023;16(6):2425. doi:10.3390/ma16062425.
31. Heimbs S, Heller S, Middendorf P, Hähnel F, Weiße J. Low velocity impact on CFRP plates with compressive preload: test and modelling. Int J Impact Eng. 2009;36(10–11):1182–93. doi:10.1016/j.ijimpeng.2009.04.006.
32. Dhaliwal GS, Newaz GM. Experimental and numerical investigation of flexural behavior of hat sectioned aluminum/carbon fiber reinforced mixed material composite beam. Compos Part B Eng. 2020;182:107642. doi:10.1016/j.compositesb.2019.107642.
33. Khan SH, Sharma AP. Progressive damage modeling and interface delamination of cross-ply laminates subjected to low-velocity impact. J Strain Anal Eng Des. 2018;53(6):435–45. doi:10.1177/0309324718780598.
34. Wang HP, Xiang P, Li X. Theoretical analysis on strain transfer error of FBG sensors attached on steel structures subjected to fatigue load. Strain. 2016;52(6):522–30. doi:10.1111/str.12195.
35. Othonos A. Fiber Bragg gratings. Rev Sci Instrum. 1997;68(12):4309–41. doi:10.1063/1.1148392.
36. Bhaskar CVN, Pal S, Pattnaik PK. Recent advancements in fiber Bragg gratings based temperature and strain measurement. Results Opt. 2021;5(5):100130. doi:10.1016/j.rio.2021.100130.
37. Wang HP, Ni YQ, Dai JG, Yuan MD. Interfacial debonding detection of strengthened steel structures by using smart CFRP-FBG composites. Smart Mater Struct. 2019;28(11):115001. doi:10.1088/1361-665X/ab3add.
38. Iqbal M, Karuppanan S, Perumal V, Ovinis M, Khan A. Stress concentration factors in CFRP-reinforced KT-joints under multiplanar bending loads: experimental and numerical investigation. Results Eng. 2025;25:103745. doi:10.1016/j.rineng.2024.103745.
39. Hopf B, Fischer B, Lindner M, Koch AW, Roths J. A three-dimensional-FEM model with experimentally determined material parameters of an FBG sensor element in a Panda-type fiber. J Lightwave Technol. 2018;36(4):1076–83. doi:10.1109/jlt.2017.2755598.
40. Khan SH, Sharma AP, Kitey R, Parameswaran V. Effect of metal layer placement on the damage and energy absorption mechanisms in aluminium/glass fibre laminates. Int J Impact Eng. 2018;119:14–25. doi:10.1016/j.ijimpeng.2018.04.011.